$BaCe_{1-x}Pd_xO_{3-\delta}$ ($0 \leq x \leq 0.1$): Redox Controlled Ingress and Egress of Palladium in a Perovskite

Jun Li,[†] Udayshankar G. Singh,[‡] Joseph W. Bennett,[§] Katharine Page,[†] James C. Weaver,[||] Jin-Ping Zhang,[†] Thomas Proffen,[⊥] Andrew M. Rappe,*[,§] Susannah Scott,*[,‡] and Ram Seshadri*[,†]

Materials Department and Materials Research Laboratory, Department of Chemical Engineering, Department of Chemistry and Biochemistry, and Department of Molecular, Cellular, and Developmental Biology, University of California, Santa Barbara, California 93106, The Makineni Theoretical Laboratories, Department of Chemistry, University of Pennsylvania, Philadelphia, Pennsylvania 19104, and Lujan Neutron Scattering Center, Los Alamos National Laboratory, LANSCE-12, MS H805, Los Alamos, New Mexico 87545

Received October 19, 2006. Revised Manuscript Received December 29, 2006

We demonstrate using a combination of X-ray and neutron diffraction and X-ray photoelectron spectroscopy that Pd^{2+} ions can be substituted for Ce in perovskite $BaCeO_3$ and that, under oxidizing conditions, $BaCe_{1-x}Pd_xO_{3-\delta}$ ($0 \leq x \leq 0.1$) compositions can be prepared. Neutron diffraction has helped verify that $\delta \approx x$, implying that Ce^{4+} ions are substituted by Pd^{2+} and that a vacancy is concurrently created on the oxygen sublattice. The structure of the host compound and models for Pd substitution have also been studied using density functional theory, which has provided a detailed *local* description of the structure. The Pd^{2+}-containing perovskite phases extrude elemental face-centered cubic palladium when heated in a reducing atmosphere. This elemental palladium is re-absorbed as ions into the perovskite lattice upon heating in flowing oxygen. Evidence for such *cyclable* ingress and egress of palladium under redox conditions is presented. A curious morphological change that results from the redox cycling of $BaCe_{1-x}Pd_xO_{3-\delta}$ is the formation of perovskite nanowires, which we believe to arise from regrowth of the perovskite around particles of elemental palladium.

Introduction

There has been great recent interest in the notion of self-regenerating or "intelligent'' catalysts: an idea presented by Nishihata et al.[1] In these catalysts, noble metals such as palladium are incorporated in their ionic state in an oxide host, where they remain under oxidizing conditions. The noble metal ions are released by the host in the form of small particles under reducing conditions, whence they display catalytic activity. Thus under conditions where the particles would sinter and lose surface area, they are re-absorbed into the perovskite lattice. Catalytic activity is recovered on exposure to a reducing atmosphere. The specific system that the authors used to perform this demonstration was the perovskite $LaFe_{0.57}Co_{0.38}Pd_{0.05}O_3$, and by performing diffraction experiments at the Pd K-edge, the authors showed that Pd is incorporated on the B site of the ABO_3 perovskite structure. In a more recent article, the same group[2] has shown that $LaFe_{0.95}Pd_{0.05}O_3$ can be cycled similarly, with reducing conditions giving rise to Pd nanoparticle formation and oxidizing conditions leading to Pd cation incorporation into the perovskite lattice. The authors determine that particle sintering and the associated loss of catalytic surface area are significantly reduced when perovskite hosts are employed, in comparison with Pd supported on the more usual Al_2O_3. Self-generating perovskite catalysts have been the subject of a recent review.[3]

In this contribution, we report a new system capable of stabilizing Pd^{2+} in relatively large quantities, nearing 10 atom %, in the B-site of the perovskite structure. The perovskite host $Ba^{2+}Ce^{4+}O_3$ (references 4 and 5) was selected on the basis of three crystal chemical principles. First, the large Ce^{+4} ion (radius = 0.87 Å in six-coordination) was selected as the host B cation so that the B-site octahedra can accommodate the large Pd^{+2} ion (radius = 0.64 Å in square planar four-coordination and 0.86 Å in six-coordination). All ionic radii quoted here are from Shannon.[6] The second is the ability of Ba^{2+} to stabilize high oxidation states on other elements, particularly in the perovskite lattice. This is a consequence of the large size of Ba^{2+}. From the bond valence net[7] for perovskite $BaBO_3$, it is observed that oxygen is obliged to

* To whom correspondence should be addressed. E-mail: rappe@sas.upenn.edu (A.M.R.), sscott@engineering.ucsb.edu (S.S.), seshadri@mrl.ucsb.edu (R.S.).
[†] Materials Department and Materials Research Laboratory, University of California.
[‡] Department of Chemical Engineering and Department of Chemistry and Biochemistry, University of California.
[§] University of Pennsylvania.
[||] Department of Molecular, Cellular, and Developmental Biology, University of California.
[⊥] Los Alamos National Laboratory.

(1) Nishihata, Y.; Mizuki, J.; Akao, T.; Tanaka, H.; Uenishi, M.; Kimura, M.; Okamoto, T.; Hamada, N. *Nature* **2002**, *418*, 164−167.
(2) Tanaka, H.; Tan, I.; Uenishi, M.; Taniguchi, M.; Kimura, M.; Nishihata, Y.; Mizuki, J. *J. Alloys Compd.* **2006**, *408*−*412*, 1071−1077.
(3) Nishihata, Y.; Mizuki, J.; Tanaka, H.; Uenishi, M.; Kimura, M. *J. Phys. Chem. Solids* **2005**, *66*, 274.
(4) Hoffmann, A. *Z. Phys. Chem. B* **1935**, *28*, 65.
(5) Jacobson, A. J.; Tofield, B. C.; Fender, B. E. F. *Acta. Crystallogr., Sect. B* **1972**, *28*, 956−961.
(6) Shannon, R. D. *Acta. Crystallogr., Sect. A* **1976**, *32*, 751−767.

10.1021/cm062500i CCC: $37.00
Published on Web 02/21/2007

obtain much of its bond valence from the B ion. Thus hard-to-attain oxidation states such as Co^{4+} can be stabilized in Ba-containing perovskites as exemplified by $BaCoO_3$.[8] The third is that the Ce^{4+}/Ce^{3+} couple could provide this host compound some redox flexibility. Substituted $BaCeO_3$ has been much studied as a proton conducting material.[9]

We unambiguously demonstrate, using a number of experimental techniques, that Pd^{2+} incorporates into the perovskite lattice, can be cycled out as face-centered cubic (fcc) Pd, and is cycled back in as Pd^{2+}, purely as a function of the heating atmosphere. The characterization techniques employed by us require relatively large substitutions (x approaching 0.1 in $BaCe_{1-x}Pd_xO_{3-\delta}$). Actual use in catalysis would not require x to be as large, and smaller substitutions are easily achieved. We do note as a caveat that $BaCe_{1-x}Pd_xO_{3-\delta}$ is by no means an ideal catalyst for use in a carbon-containing atmosphere given the notorious stability and ease of formation of $BaCO_3$. When Pd^{2+} is incorporated into the perovskite lattice, it creates a vacancy on the oxygen sublattice, and this is indeed found in the neutron structure refinement. Thus $\delta \approx x$ in $BaCe_{1-x}Pd_xO_{3-\delta}$. Density functional theory (DFT) has been used to model the substitution of Pd^{2+} in the Ce^{4+} site with an accompanying oxygen vacancy to obtain a picture of the local structure around Pd^{2+} in the perovskite structure. Insights as to how a square planar ion such as Pd^{2+} is accommodated in a normally octahedral site emerge. The structural description for substitution obtained from DFT has been compared with the experimental neutron pair distribution function (PDF).

Experimental Section

$BaCe_{1-x}Pd_xO_{3-\delta}$ ($0 \le x \le 0.1$) perovskite samples were prepared by grinding together BaO_2 (99%, Cerac), CeO_2 (99.9%, Cerac), and PdO (99.95%, Cerac) in appropriate stoichiometric ratios, pelletizing the ground powders, and heating in flowing oxygen at 1000 °C for 10 h. BaO_2 was used as a Ba source in preference to other compounds because it obviates the use of the hard-to-decompose carbonate and is less hygroscopic than BaO. The pellets were then reground, pelletized, and heated for a further 10 h at 1000 °C in flowing oxygen. The as-prepared samples are also referred to as oxidized samples. Palladium metal could also be used in place of PdO for the reactions, although most of the preparations reported here were performed with the latter. The reduction reactions were carried out in flowing $5\%H_2/95\%N_2$ at different temperatures up to 1000 °C for 1 h or longer; the term reduction as used here is always associated with flowing $5\%H_2/95\%N_2$. The oxidized samples were reduced both in pellet and in powder form.

Powder X-ray diffraction (XRD) data were acquired on a Philips XPERT MPD X-ray diffractometer with Cu Kα radiation at room temperature. X-ray profiles were subject to Rietveld analysis using the XND Rietveld code.[10] Time-of-flight neutron diffraction data were collected at room temperature on the neutron powder diffractometer NPDF[11] at the Lujan Neutron Scattering Center at the Los Alamos Neutron Science Center. Samples of approximately 1 g were contained in vanadium cans for the experiments. Diffraction data were analyzed with the Rietveld method as embodied in the GSAS-EXPGUI[12] suite of programs. Bond valence analysis of the structures obtained from neutron diffraction made use of the Bond Valence Calculator.[13]

X-ray photoelectron spectroscopy (XPS) spectra were obtained on a Kratos Axis Ultra spectrometer with a monochromatic Al Kα source ($E = 1486$ eV). Samples were mounted on a stainless steel sample holder using double-sided carbon tabs. The residual pressure inside the analysis chamber was below 1×10^{-9} Torr. Survey spectra over wide ranges of binding energy were acquired using an analyzer pass energy of 160 eV, and higher-resolution spectra of Pd 3d and Ce 3d levels were acquired at 40 eV pass energy. The C 1s peak from adventitious hydrocarbon, expected at 284.8 eV binding energy, was used to correct the binding energy for sample charging effects. Binding energies were measured with a precision of ±0.2 eV.

Secondary electron field emission scanning electron microscopy (SEM) was performed on Sirion XL40 and XL30 microscopes and scanning energy dispersive X-ray (EDX) images were recorded on a Tescan Vega TS5130MM microscope with a model 500 EDS by IXRF Systems. High-resolution images and Z-contrast images were obtained on a field emission transmission electron microscope operated at 300 kV (FEI Tecnai F30UT, $C_S = 0.52$ mm) in conventional high-resolution transmission electron microscopy (TEM) and scanning transmission electron microscopy (STEM) modes. A high-angle annular dark-field detector was used for STEM imaging. In combination with an EDX detector (EDAX-R, 135 eV), chemical analysis with nanometric electron probes was performed.

Computational Methods

An in-house solid-state DFT code used in previous studies[14,15] was employed to relax the ionic positions and optimize lattice constants. The generalized gradient approximation (GGA)[16] of the exchange correlation functional and a $4 \times 4 \times 4$ Monkhorst−Pack[17] sampling of the Brillouin zone were used for all calculations. All atoms were represented by norm-conserving optimized[18] designed nonlocal[19] pseudopotentials. All pseudopotentials were generated with the OPIUM code.[20] The calculations were performed with a plane wave cutoff of 50 Ry. Calculations on $BaCeO_3$ and $BaCeO_3$ with Pd substituting for Ce were performed on 40 atom unit cells in a $2 \times 2 \times 2$ supercell of the cubic perovskite. The superlattice allows for three-dimensional octahedral tilting that is seen in experiment. For the Pd-substituted perovskite, three supercells of composition

(7) Brown, I. D. *The Chemical Bond in Inorganic Chemistry, The Bond Valence Model*; IUCr Monographs on Crystallography 12; Oxford University Press: New York, 2002.
(8) Yamaura, K.; Zandbergen, H. W.; Abe, K.; Cava, R. J. *J. Solid State Chem.* **1999**, *146*, 96−102.
(9) Kreur, K. D. *Annu. Rev. Mater. Res.* **2003**, *33*, 333−359.
(10) Bérar, J.-F.; Baldinozzi, G. *International Union of Crystallography−Commission on Powder Diffraction Newsletter* **1998**, *20*, 3−5.
(11) Proffen, T.; Egami, T.; Billinge, S. J. L.; Cheetham, A. K.; Louca, D.; Parise, J. B. *Appl. Phys. A* **2002**, *74*, s163−s165.
(12) Larson, A. C; Von Dreele, R. B. *General Structure Analysis System (GSAS)*; Los Alamos National Laboratory Report LAUR; Los Alamos National Laboratory: Los Alamos, NM, 1994; pp 86−748. Toby, B. H. *J. Appl. Crystallogr.* **2001**, *34*, 210−213.
(13) Hormillosa, C.; Healy, S.; Stephen, T.; Brown, I. D. *Bond Valence Calculator*, Version 2.0; McMaster University, Canada, 1993 (http://ccp14.ac.uk).
(14) Mason, S. E.; Grinberg, I.; Rappe, A. M. *Phys. Rev. B* **2004**, *69*, 161401(1−4).
(15) Bennett, J. W.; Grinberg, I.; Rappe, A. M. *Phys. Rev. B* **2006**, *73*, 180102(1−4).
(16) Perdew, J. P.; Burke, K.; Ernzerhof, M. *Phys. Rev. Lett.* **1996**, *77*, 3865−3868.
(17) Monkhorst, H. J.; Pack, J. D. *Phys. Rev. B* **1976**, *13*, 5188−5192.
(18) Rappe, A. M.; Rabe, K. M.; Kaxiras, E.; Joannopoulos, J. D. *Phys. Rev. B* **1990**, *41*, 1227−1230.
(19) Ramer, N. J.; Rappe, A. M. *Phys. Rev. B* **1999**, *59*, 12471−12478.
(20) http://opium.sourceforge.net, version 2.02, 2005.

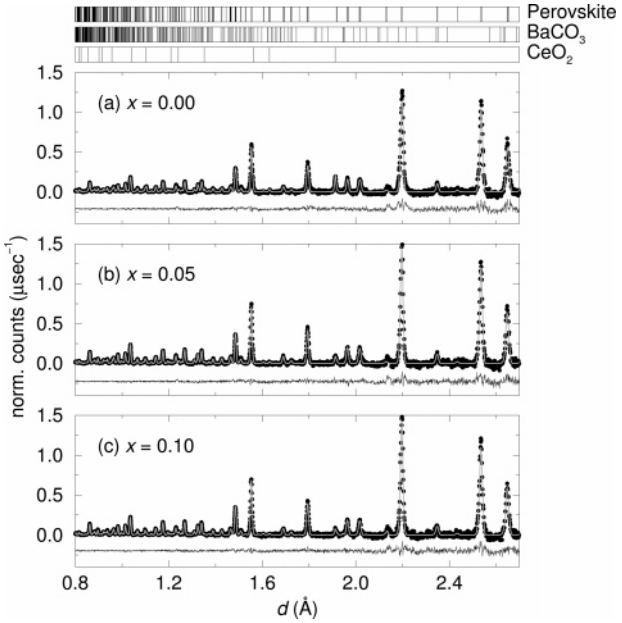

Figure 1. Rietveld refinement of the highest-resolution banks of time-of-flight neutron diffraction data acquired on $BaCe_{1-x}Pd_xO_{3-\delta}$ phases with the compositions (a) $x = 0.00$, (b) $x = 0.05$, and (c) $x = 0.10$. The filled circles are data, and the gray lines are the Rietveld fit. Vertical lines at the top of the figure are the expected peak positions for the orthorhombic perovskite and two impurity phases, $BaCO_3$ and CeO_2.

$Ba_8Ce_7PdO_{23}$, corresponding to a 12.5% Pd^{2+} for Ce^{4+} substitution, were studied, with the oxygen vacancy located in different positions in the structure with respect to Pd and Ce. Below, we concentrate on the lowest-energy structure, with the oxygen vacancy near Pd.

Results and Discussion

Structure and Substitution. $BaCe_{1-x}Pd_xO_{3-\delta}$ samples with $x = 0.00$, 0.05, and 0.10 were prepared in approximately 1−2 g batches at 1000 °C under flowing O_2, heating twice for 10 h with an intermediate grinding. The samples ranged in color from off-white for $x = 0.00$ to a dark yellow-brown with a green tinge for $x = 0.10$. Time-of-flight neutron diffraction data, displayed for the highest-resolution bank (bank 4, ±148°) with Rietveld fits in Figure 1, correspond to nearly phase pure orthorhombic perovskites.[5] The very high data quality made evident small amounts of impurities, namely, cubic CeO_2 and orthorhombic $BaCO_3$ in all three phases, and these were included in the refinements. However, the relative phase amounts of these were nearly negligible as suggested by quantitative phase analysis. In the many samples prepared and studied by X-ray diffraction, these second phases were not observed, and they are thought to arise from the larger amounts of samples prepared for the neutron experiments. Crystal structure data obtained for the three phases are summarized in Table 1. A small contraction of 0.16% of the unit cell volume upon substitution of Ce by Pd was observed on going from $x = 0$ to $x = 0.10$. Refinements of the amount of oxygen on the two sites in the *Pnma* structure, as well as the ratio of Ce to Pd on the B site, were stable. To within 1 atom %, the compositions for $x = 0.00$, 0.05, and 0.10 are respectively $BaCeO_{3.00}$, $BaCe_{0.95}Pd_{0.05}O_{2.95}$, and $BaCe_{0.90}Pd_{0.10}O_{2.90}$. Further evidence that Pd substitutes for Ce comes from the observed

Table 1. Crystal Structures of $BaCe_{1-x}Pd_xO_3$ As Obtained from Rietveld Refinement of Time-of-Flight Neutron Diffraction Data on Powders[a]

parameter	$x = 0.00$	$x = 0.05$	$x = 0.10$
R_p (%)	1.13	1.20	1.19
wR_p (%)	1.60	1.65	1.67
χ^2	2.11	1.39	1.38
a (Å)	6.2140(1)	6.2120(2)	6.2118(2)
b (Å)	8.7741(1)	8.7753(2)	8.7742(2)
c (Å)	6.2334(1)	6.2269(1)	6.2268(1)
V (Å^3)	339.86(1)	339.44(1)	339.38(1)
Ba, x	0.0204(5)	0.0192(4)	0.0188(4)
Ba, z	−0.0085(7)	−0.0054(6)	−0.0048(6)
O1, x	−0.0094(7)	−0.0118(6)	−0.0120(6)
O1, z	0.4287(4)	0.4282(3)	0.4264(3)
O2, x	0.2790(3)	0.2773(3)	0.2765(2)
O2, y	0.0384(2)	0.0382(2)	0.0380(2)
O2, z	0.7235(3)	0.7235(2)	0.7237(3)
Ce (occ.)	0.995(6)	0.958(3)	0.906(3)
Pd (occ.)	0	0.042(3)	0.094(3)
O1 (occ.)	1.07(1)	0.981(6)	0.972(6)
O2 (occ.)	0.970(8)	0.978(4)	0.963(4)
BVS(Ba)	1.70	1.70	1.70
BVS(Ce)	4.01	4.02	4.03
BVS(Pd)		1.80	1.80
BVS(O1)	1.89	1.91	1.91
BVS(O2)	1.91	1.90	1.90

[a] Bond valence sums (BVS) were calculated using the bond valence calculator.[13] Space group *Pnma* (No. 62): Ba at x, 1/4, z; Ce, Pd at 0, 0, 1/2; O1 at x, 1/4, z; and O2 at x, y, z.

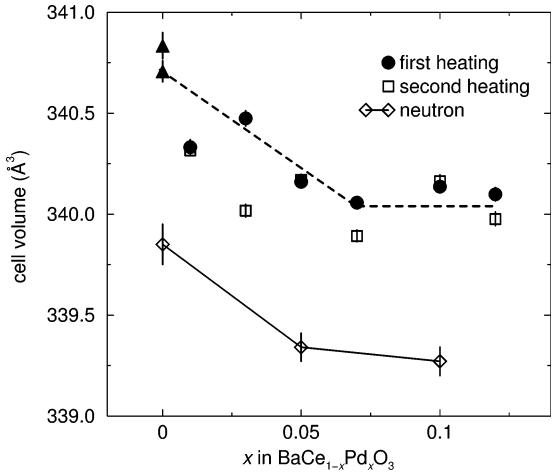

Figure 2. Evolution of the unit cell volume of perovskite $BaCe_{1-x}Pd_xO_{3-\delta}$ as a function of substitution x. Results from laboratory X-ray as well as neutron diffraction are displayed. The solid triangles at $x = 0$ display data for different preparations of $BaCeO_3$ and indicate variations between different preparations and data runs.

contraction of the BO_6 octahedron, which results in an effective increase in the bond valence sum of Ce with substitution. The bond valence of Pd is significantly less than 2, which points to the inadequacy of crystallographic models for the substitution.

A number of intermediate x compositions in $BaCe_{1-x}Pd_xO_{3-\delta}$ were also prepared, and their powder X-ray diffraction profiles were subjected to Rietveld analysis, to verify phase purity and to obtain accurate lattice parameters. The evolution of the cell volume of $BaCe_{1-x}Pd_xO_{3-\delta}$ with x, obtained from the neutron experiments as well as laboratory X-ray data, is displayed in Figure 2. The very small change in cell volume upon substitution of Ce by Pd results in the data being somewhat scattered. Experiment to experiment variations were also seen during the different preparative runs

Table 2. Comparison of the Experimental (Neutron Rietveld) Cell Parameters of $BaCeO_3$ with the Values Obtained from DFT Calculations

	experiment	calculation	% difference
a (Å)	6.214	6.284	−1.13
b (Å)	8.774	8.807	−0.34
c (Å)	6.233	6.305	−1.15

and between the laboratory X-ray and neutron data. As we suggest further on, the substitution of Pd for Ce in the perovskite is aliovalent and is accompanied by a loss of oxygen. We do not therefore expect a simple Végard-like trend in the cell volume. The purpose of Figure 2 is simply to demonstrate the effect of the substitution on the cell parameter and to suggest that, by itself, it cannot be taken for evidence of substitution.

Computational Modeling. The computed 40-atom $BaCeO_3$ unit cell was found to be symmetry reducible to the *Pnma* structure, and the cell parameters obtained for the optimized parent $BaCeO_3$ were found to be nearly within 1% of the experimental structure. The comparison of experimental and computed cell parameters is made in Table 2. DFT-GGA is seen to very slightly overestimate all three cell parameters. Structural details, such as the precise mode of tilting of the CeO_6 octahedra also closely correspond to experiment. The close agreement provides confidence for the ability of DFT to accurately model the local structure of Pd-substituted $BaCeO_3$ as well. Here we describe the essential features of one such model, an eight-formula unit supercell ($2 \times 2 \times 2$) where one of the Ce^{4+} was substituted by Pd^{2+}, and in addition, an oxygen vacancy was created to account for the aliovalent nature of the substitution, consistent with the neutron refinement. The optimized structure is displayed in Figure 3. The tilting of CeO_6 octahedra in this highly distorted perovskite (a tolerance factor of 0.94 for $BaCeO_3$) is clearly seen. Creating oxygen vacancy in an ABO_3 would normally mean creating two BO_5 square pyramids per vacancy. In the optimized structure described here, the very strong tendency of square planarity of d^8 Pd^{2+} is satisfied by the marked tilting of the neighboring CeO_5 square pyramid so that the distance between the Pd^{2+} and its fifth O (the capping O on the CeO_5 square pyramid) is increased to 2.66 Å. In contrast, the four proximal (square planar) O atoms are at a distance to Pd^{2+} of 2.05 Å. The substitution of Pd^{2+} for Ce^{4+} is found in the computation to result in a decreased unit cell volume, in agreement with experiment. The contraction is however much larger in the calculation, of the order of 2.6%, for the 12.5% substitution, as opposed to a 0.16% contraction seen in experiment for the 10% substitution.

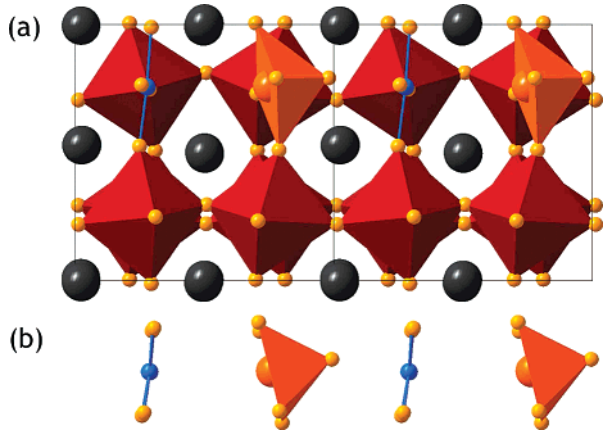

Figure 3. (a) Two unit cells of the crystal structure of $Ba_8Ce_7PdO_{23}$, equivalent to $BaCe_{0.875}Pd_{0.125}O_{2.875}$, optimized by density functional calculations. The large gray spheres are Ba^{2+}, small yellow spheres are oxygen, and cyan spheres are Pd^{2+}. CeO_6 octahedra are displayed in red. The oxygen vacancy is proximal to Pd^{2+} and creates, in addition, some CeO_5 square pyramids (dark orange). (b) The tilting of the CeO_5 square pyramids is clearly seen to result in Pd^{2+} being square planar rather than square-pyramidal.

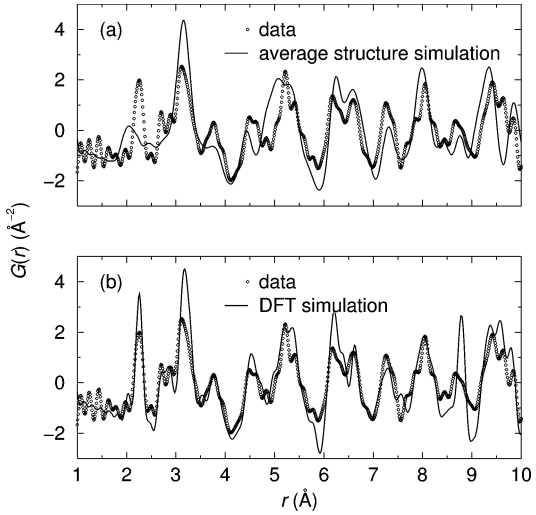

Figure 4. (a) Experimental neutron PDF $G(r)$ of $BaCe_{1-x}Pd_xO_{3-\delta}$ with $x = 0.10$ (data points) compared with the PDF simulated from the average (Rietveld) structure and (b) experimental $G(r)$ compared with the PDF simulated using the DFT model of $Ba_8Ce_7PdO_{23}$ as described in the previous figure.

The neutron powder diffractometer[11] is capable of a very large range of momentum transfer, and the data can be used to obtain PDFs $G(r)$, permitting the local structure to be modeled.[21] We have extracted from the total neutron scattering the PDF $G(r)$ for the $x = 0.10$ sample, and this is shown as data points in the panels of Figure 4. In panel a, a simulation of the PDF from the average (Rietveld) structure of $BaCe_{0.90}Pd_{0.10}O_{2.90}$ is shown as a gray line. This simulation clearly fails badly in modeling the data at all r ranges, with strong disagreement for short lengths. The $2 \times 2 \times 2$ structural model described in Figure 3, with the composition $Ba_8Ce_7PdO_{23}$, was used as a model in the program PDFFIT[22] to simulate $G(r)$, shown in panel b. No attempt was made to refine the lattice parameters or the positional parameters in this *P*1 structure, of which there are 117 from 39 atoms. Despite this, the correspondence between experiment and computation is very encouraging, especially for short r. In particular, the precise peak locations are remarkably well matched. This is strong evidence for consistency between the DFT model and the experiment. Because the DFT calculations were performed on a cell with edges near 8 Å, it is to be expected that at longer r, the comparison between experiment and computation is less satisfactory.

(21) Billinge, S. J. L.; Egami, T. *Underneath the Bragg Peaks: Structural Analysis of Complex Materials*; Pergamon Press Elsevier: Oxford, U.K., 2003.
(22) Proffen, Th.; Billinge, S. J. L. *J. Appl. Cryst.* **1999**, *32*, 572−575.

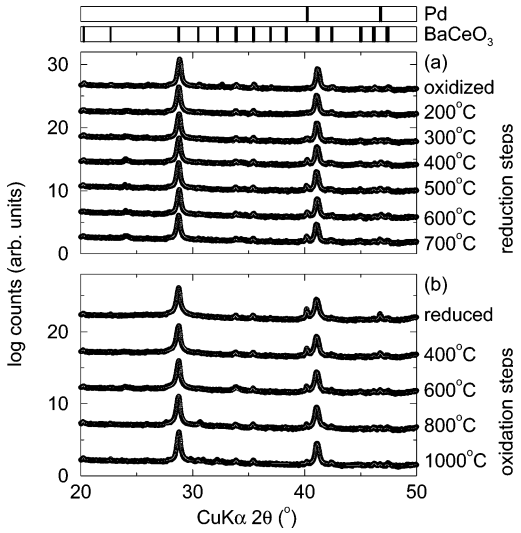

Figure 5. (a) Laboratory XRD patterns (filled circles) and Rietveld fit (gray lines) for a fully oxidized $BaCe_{1-x}Pd_xO_{3-\delta}$ sample with $x = 0.10$ (topmost trace) and the diffraction patterns obtained on treating different batches of this sample at the different indicated temperatures for 1 h under flowing $5\%H_2/95\%N_2$. The emergence of the principal 111 reflection of fcc Pd near 41° 2θ with increasing the temperature should be noted. (b) Diffraction patterns and Rietveld fit corresponding to the effect of successive heating of a single two-phase perovskite + fcc Pd sample (labeled "reduced'') in flowing O_2 at the different indicated temperatures. Note the reduction in the intensity of the fcc Pd peak with increasing oxidation temperature. All XRD data are displayed on a semi-logarithmic scale. Vertical lines at the top of the plot indicate expected peak positions.

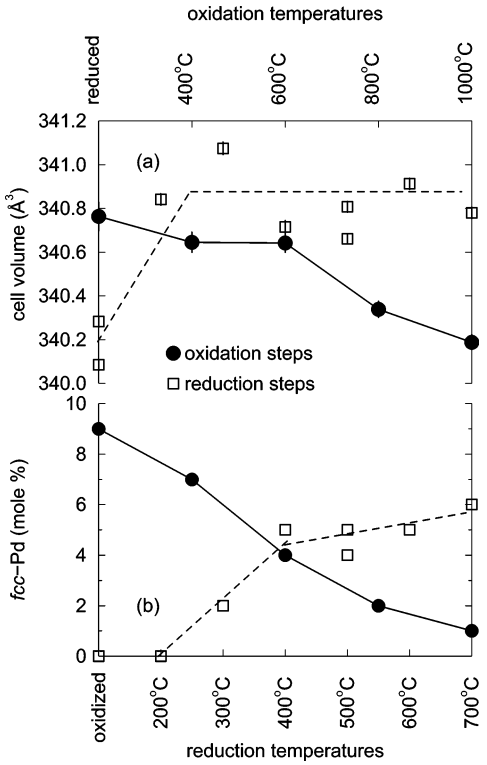

Figure 6. (a) Perovskite cell volume as a function of the different temperatures at which $BaCe_{1-x}Pd_xO_{3-\delta}$ with $x = 0.10$ was reduced and as a function of different temperatures at which a reduced, two-phase fcc Pd and perovskite sample was oxidized. (b) Corresponding mole amounts in percent, of fcc Pd, obtained from two-phase Rietveld refinements. The lines are guides to the eye.

Ingress and Egress of Palladium. To establish that palladium enters, can be removed, and then can be reinserted into the perovskite lattice, we performed a series of heating experiments on samples with the $x = 0.10$ composition. Panel a of Figure 5 displays X-ray diffraction data showing evidence for the egress of palladium from the perovskite lattice. The data, shown as points, and the Rietveld fits, shown as gray lines, are plotted using the natural logarithm of the counts as the ordinate. Starting with an oxidized (meaning as-prepared) $BaCe_{1-x}Pd_xO_{3-\delta}$, $x = 0.10$, sample, shown in the uppermost trace, the results of heating this sample, *in separate batches*, under flowing $5\%H_2/95\%N_2$ for 1 h periods at the indicated temperatures, are displayed. We chose to do the reduction experiments in separate batches because the same samples were also studied by XPS. The emergence of the 111 reflection of fcc Pd near 41° 2θ upon reduction is clearly observed. Panel b of Figure 5 shows conversely the ingress of palladium after it has been extruded out of the lattice. We started with a fully reduced sample, formed by heating $BaCe_{1-x}Pd_xO_{3-\delta}$ with $x = 0.10$ at 1000 °C for 10 h, shown in the uppermost trace. Heating this sample in flowing O_2 for 1 h periods at the different indicated temperatures resulted in the gradual disappearance of the reflections corresponding to fcc Pd, providing evidence for the ingress of Pd. Note that the oxidations shown here were performed in a successive manner on the *same* starting two-phase (perovskite and fcc Pd) sample.

Rietveld refinements of the diffraction data displayed in the previous figure allowed cell volumes and relative phase fractions of fcc Pd and perovskite to be obtained, which could be used to monitor the egress and ingress of palladium. The cell volume, plotted in Figure 6a, shows that the egress of palladium from $BaCe_{1-x}Pd_xO_{3-\delta}$ with $x = 0.10$ upon heating in $5\%H_2/95\%N_2$ (reduction) is rapid, with the volume increasing, presumably due to Pd being extruded from the perovskite lattice. The volume expansion is seen after only 1 h at 200 °C. It is seen from panel b that indeed fcc Pd has made a quantifiable appearance after 1 h at 300 °C. Upon heating at 700 °C for 1 h under $5\%H_2/95\%N_2$, about half the Pd^{2+} has come out of the lattice as elemental fcc Pd. Ingress of palladium is much more sluggish. It is seen from changes in the cell volume in Figure 6a that it is only after heating the fully reduced sample *successively* in flowing O_2 for 1 h periods at 400 °C, 600 °C, 800 °C, and 1000 °C that the cell volume recovers to that of the fully oxidized sample. Correspondingly, from panel b of this figure, almost no fcc Pd is observed after such extensive oxidation. The greater scatter in the data sets corresponding to reduction in this figure should be noted and arises from reductions being carried out on separate sample batches. On the other hand, all oxidation data were acquired on the same sample.

The cyclability of the ingress and egress has been followed for a sample of $BaCe_{1-x}Pd_xO_{3-\delta}$ with $x = 0.07$. We show in Figure 7a that the as-prepared nearly single phase sample can be reduced (10 h at 1000 °C under flowing $5\%H_2/95\%N_2$) to two phases with fcc Pd appearing, oxidized back to a single-phase perovskite (10 h at 1000 °C under flowing O_2) and so on. In panel b the changes in cell volume obtained from the Rietveld refinement are monitored, and as expected from the data shown in the previous figures, reduction results in egress of palladium and an enhancement of the cell volume. Quantitative phase analysis suggested

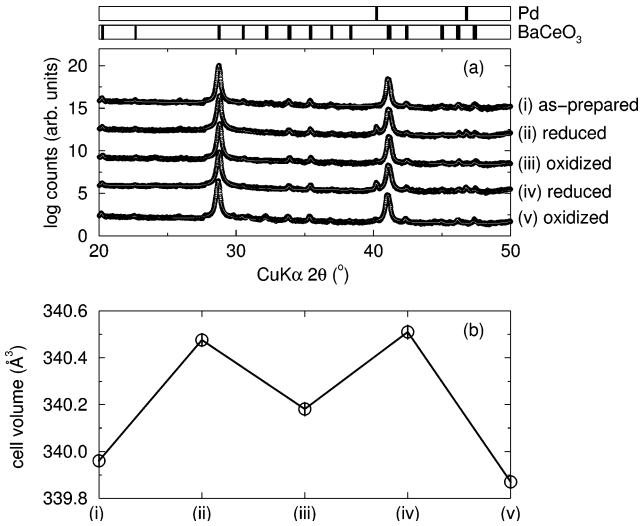

Figure 7. (a) XRD patterns and one- or two-phase Rietveld fits of $BaCe_{1-x}Pd_xO_{3-\delta}$ samples with $x = 0.07$ subject successively to reduction and oxidation as described in the text. (b) Corresponding unit cell volumes from the Rietveld refinements.

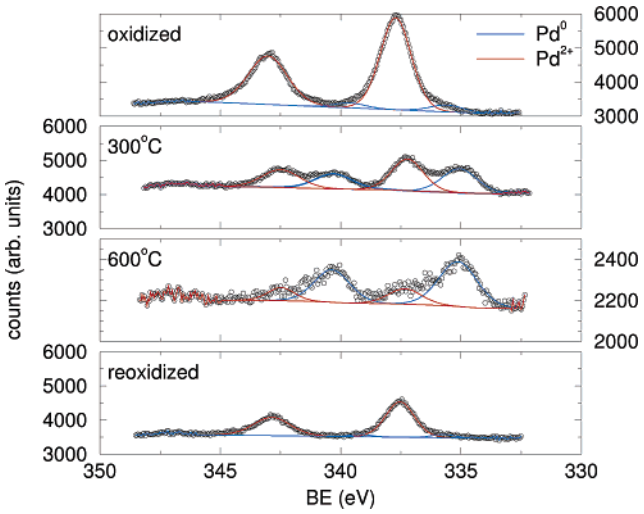

Figure 8. Al Kα XPS spectra in the palladium 3d region of $BaCe_{1-x}Pd_xO_{3-\delta}$ with $x = 0.10$ (labeled "oxidized'') and the spectra obtained after reduction at the different indicated temperatures. The bottom-most spectrum corresponds to the sample reoxidized to $BaCe_{1-x}Pd_xO_{3-\delta}$. Fits to doublets corresponding to Pd^0 and Pd^{2+} are shown.

that, under the conditions used, the relative phase amount of fcc Pd was only near 4 mol %.

XPS Studies. We have monitored the ingress and egress of palladium in the perovskite using core-level XPS. The Pd 3d levels could be resolved into sets of spin−orbit doublets: Pd ($3d_{5/2}$ and $3d_{3/2}$). We verified (data not displayed) peak positions of 335.4 and 340.5 eV for Pd metal and peak positions of 336.7 and 342.0 eV for PdO, consistent with values reported in the literature.[23]

Figure 8 displays XPS spectra acquired on various oxidized and reduced samples of $BaCe_{1-x}Pd_xO_{3-\delta}$ with $x = 0.10$ in the region of palladium 3d binding energies. The uppermost panel, labeled oxidized, displays the XPS spectrum of $BaCe_{1-x}Pd_xO_{3-\delta}$. Peaks due to cationic Pd^{2+} appear at 337.7 and 343.0 eV, shifted to higher binding energy by 1.0 eV with respect to PdO. This shift toward higher binding energy suggests a very ionic environment for Pd^{2+} ions, such as would be obtained in the B-site of the perovskite structure. While Nishihata and co-workers[1,2] interpret the shifted binding energies of palladium in perovskites as corresponding to Pd^{3+}, we interpret that Pd^{2+} in $BaCe_{1-x}Pd_xO_{3-\delta}$ is simply more ionic than Pd^{2+} in PdO. Indeed, the extended X-ray absorption fine structure Pd−O coordination reported by Tanaka et al.[2] for Pd in $LaFe_{0.95}Pd_{0.05}O_3$, six oxygen neighbors at a distance of 2.04 Å, yields a bond valence sum on Pd of 2.2, consistent with our interpretation of Pd^{2+}. The uppermost spectrum in Figure 8 also shows a doublet with binding energies of 335.1 and 340.3 eV, close to what is expected for elemental Pd. Quantitative analysis based on Scofield photoionization cross sections[24] shows that 92% of the palladium is in ionic form, whereas 8% of the palladium is in the elemental form. When similar data are acquired on the $BaCe_{1-x}Pd_xO_{3-\delta}$ sample with $x = 0.05$, no evidence for Pd^0 is obtained. This suggests, in agreement with the X-ray cell volume variation, that the solubility limit of Pd^{2+} in the perovskite is close to 10 atom %.

XPS spectra in the Pd 3d region acquired on reduction products obtained by treating this sample in different batches under flowing $5\%H_2/95\%N_2$ at 300 °C and 600 °C (1 h duration) are also displayed in this figure. After the 300 °C reduction, there is a significant increase in the signal from Pd^0. In the sample treated at 600 °C, there is almost no signal from Pd^{2+}, but the signal from Pd^0 is much weaker. The curious suppression of the signal from elemental Pd, which we know from X-ray diffraction to exist in significant quantities in this sample, is thought to be associated with the tendency of the perovskite to overgrow the elemental palladium. In addition, if we try and balance the equation for the reduction of the $x = 0.10$ sample and assume stoichiometric $BaCeO_3$ as one of the products, we have

$$BaCe_{0.90}Pd_{0.10}O_{2.90} + 0.10H_2 \xrightarrow{\text{reduce}} 0.90BaCeO_3 + 0.10Pd + 0.10BaO + 0.10H_2O$$

There is no evidence for BaO in the products from X-ray diffraction. However, BaO is highly hygroscopic and is likely to form a combination of poorly crystalline hydroxides and carbonates which are effectively X-ray invisible. These products could segregate to the surface and cover the freshly formed fcc Pd resulting in the decreased XPS intensity. Such coverage of the metal surface by oxides is in keeping with the high surface energies of metals. We address some of these issues again with microscopy. Reoxidation of the reduced sample in flowing O_2 for 1 h at 1000 °C resulted in the bottom-most XPS spectrum, with the Pd^0 signal almost completely suppressed and, correspondingly, the Pd^{2+} signal having grown in strength.

We also carried out XPS studies in the region of the Ce 3d binding energies. In Figure 9 XPS spectra of samples of $BaCe_{1-x}Pd_xO_{3-\delta}$ with $x = 0.10$ are displayed before and after reduction. The different cerium peaks were assigned fol-

(23) Brun, M.; Berthet, A.; Bertolini, J. C. *J. Electron Spectrosc. Relat. Phenom.* **1999**, *104*, 55−60. Priolkar, K. R.; Bera, P.; Sarode, P. R.; Hegde, M. S.; Emura, S.; Kumashiro, R.; Lalla, N. P. *Chem. Mater.* **2002**, *14*, 2120−2128.

(24) Scofield, J. H. *J. Electron Spectrosc. Relat. Phenom.* **1976**, *8*, 129−137.

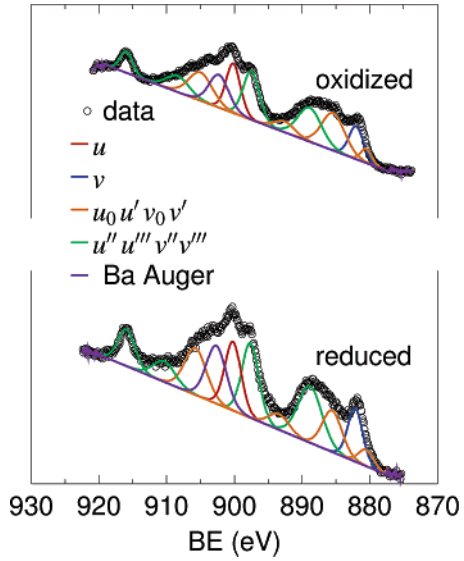

Figure 9. Al Kα XPS spectra in the cerium 3d region of as-prepared $BaCe_{1-x}Pd_xO_{3-\delta}$ with $x = 0.10$ (labeled "oxidized'') and after reduction in $5\%H_2/95\%N_2$. Data have been fitted to contributions from cerium $3d_{3/2}$ (marked by the different v's) and $3d_{5/2}$ (marked by the different u's). We have followed the nomenclature of Romeo et al.[25] in assigning the different peaks. The two sets of doublets, u_0, u' and v_0, v', correspond to Ce^{3+}, and the two sets of triplets, u, u'', u''' and v, v'', v''', correspond to Ce^{4+}. In addition, an Auger line of barium appears in this energy range.

lowing the work of Romeo et al.[25] as explained in the caption of the figure. We observe that both the oxidized and reduced samples have almost the same relative ratios of Ce^{3+} and Ce^{4+}, and given that bond valence analysis of the neutron structure suggested only Ce^{4+} in the oxidized sample, we attribute the observation of Ce^{3+} to species on the surface.

Microscopy. The two panels of Figure 10 display SEM micrographs of $BaCe_{1-x}Pd_xO_{3-\delta}$ with $x = 0.10$ showing (a) as-prepared powders and (b) powders obtained after heating under flowing $5\%H_2/95\%N_2$ for 10 h at 1000 °C. While panel a displays a morphology typical of ceramic powders, panel b shows, curiously, nanowire-like architectures. These features were not prevalent in every part of all samples but rather were found in clusters as shown here. The morphology of most of the sample was unchanged upon reduction. Our initial interpretation was that the nanowires were of fcc Pd. Indeed, a report by Ramesh and co-workers[26] suggested that depositing perovskite $La_{0.5}Sr_{0.5}FeO_3$ thin films by laser ablation in a reducing atmosphere resulted in a disproportionation to layered $LaSrFeO_4$ and Fe nanowires. Additionally, the occurrence of such wires was much more frequent when $BaCe_{1-x}Pd_xO_{3-\delta}$ samples with $x = 0.10$ were reduced, compared with samples with $x = 0.05$. However, if a large numbers of Pd nanowires are formed and exposed [as suggested by Figure 10(b)] then they would correspondingly display strong peaks in the XPS spectra in the region of the Pd^0 binding energy. This is in contrast with the rather weak signals from Pd^0 that were observed in the XPS of reduced samples. The morphologies of pure $BaCeO_3$ prepared under

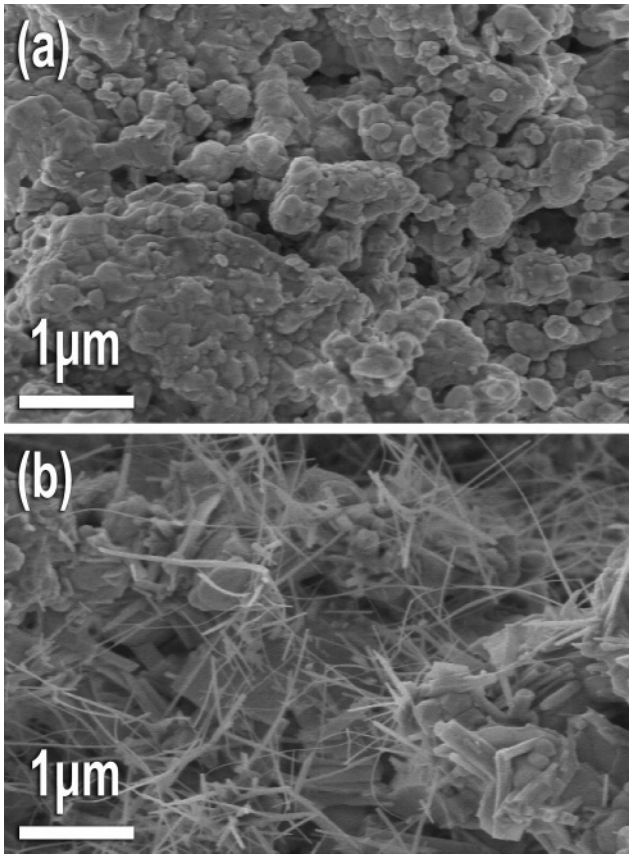

Figure 10. SEM micrographs of (a) as-prepared $BaCe_{1-x}Pd_xO_{3-\delta}$ ($x = 0.10$) and (b) after reduction in $5\%H_2/95\%N_2$ showing the development of nanowire features.

similar conditions, both before and after reduction, were also studied by us using SEM. Pure $BaCeO_3$ shows no change in microstructure upon heating under these conditions and shows no evidence of any sort of nanowire formation. The change on going from $BaCeO_3$ to $BaCe_{1-x}Pd_xO_{3-\delta}$ is that the grain size becomes smaller. No wire-like structures are seen.

To locate palladium in the sample and examine the nature of the wires, the EDX signals of Ba, Ce, and Pd were used to create chemical maps of the reduced $BaCe_{1-x}Pd_xO_{3-\delta}$, $x = 0.10$, sample. Panel a of Figure 11 displays a SEM image of a reduced sample with some wires being seen interspersed with the powders, in the middle left and upper parts of the image. Maps of this image using characteristic Ba and Ce emissions suggested that these elements are evenly distributed in the sample and are nearly equal in abundance. The inset is a map of Pd emission in the EDX spectrum, suggesting that while Pd is not as evenly distributed, there is no particular association of the wire-like features with Pd. Panel b of this image shows the circled region in panel a in higher magnification, with the wires being seen clearly at this higher magnification. The results suggest that the wires are not Pd but could be the $BaCeO_3$ perovskite, regrown in some manner as a result of heat treatment in a reducing atmosphere and in the presence of elemental Pd.

The nature of the wires was further probed using TEM in its various modes, including EDX analysis in STEM mode. Figure 12a displays a few of the wires in TEM. It is seen that the wires are as thin as a few tens of nanometers and

(25) Romeo, M.; Bak, K.; El Fallah, J.; Le Normand, F.; Hilaire, L. *Surf. Interface Anal.* **1993**, *20*, 508−512.
(26) Mohaddes-Ardabili, L.; Zheng, H.; Ogale, S. B.; Hannoyer, B.; Tian, W.; Wang, J.; Lofland, S. E.; Shinde, S. R.; Zhao, T.; Jia, Y.; Salamanca-Riba, L.; Schlom, D. G.; Wuttig, M.; Ramesh, R. *Nat. Mater.* **2004**, *3*, 533−538.

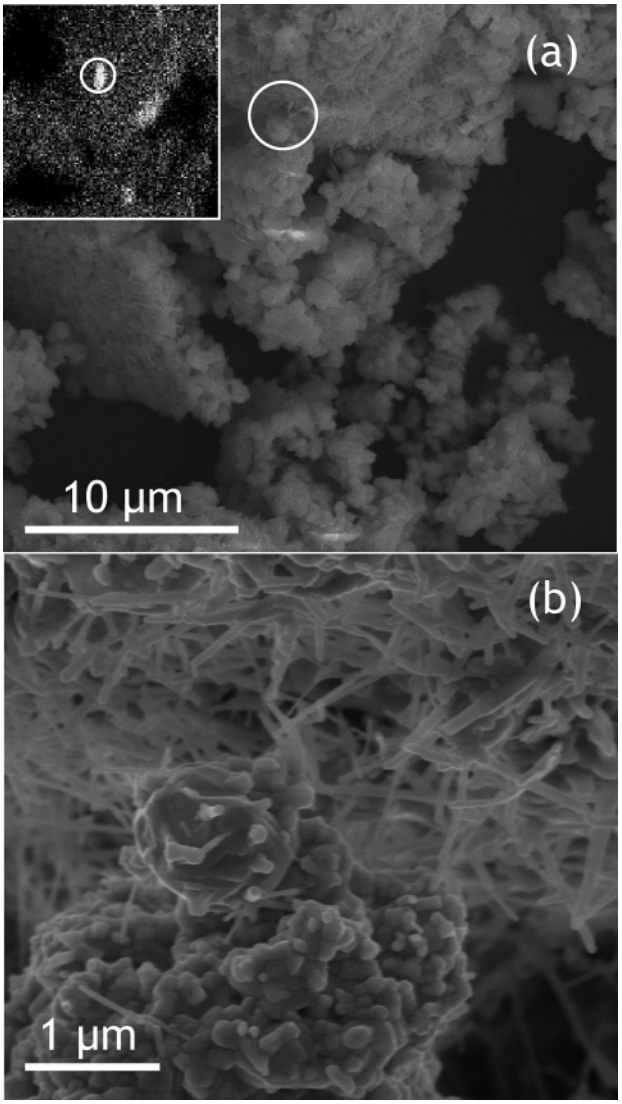

Figure 11. (a) SEM micrograph of a sample of reduced $BaCe_{1-x}Pd_xO_{3-\delta}$ with $x = 0.10$. The inset is an EDX scan of the signal from Pd, with white pixels corresponding to palladium rich regions. (b) An expanded view of the region circled in part a.

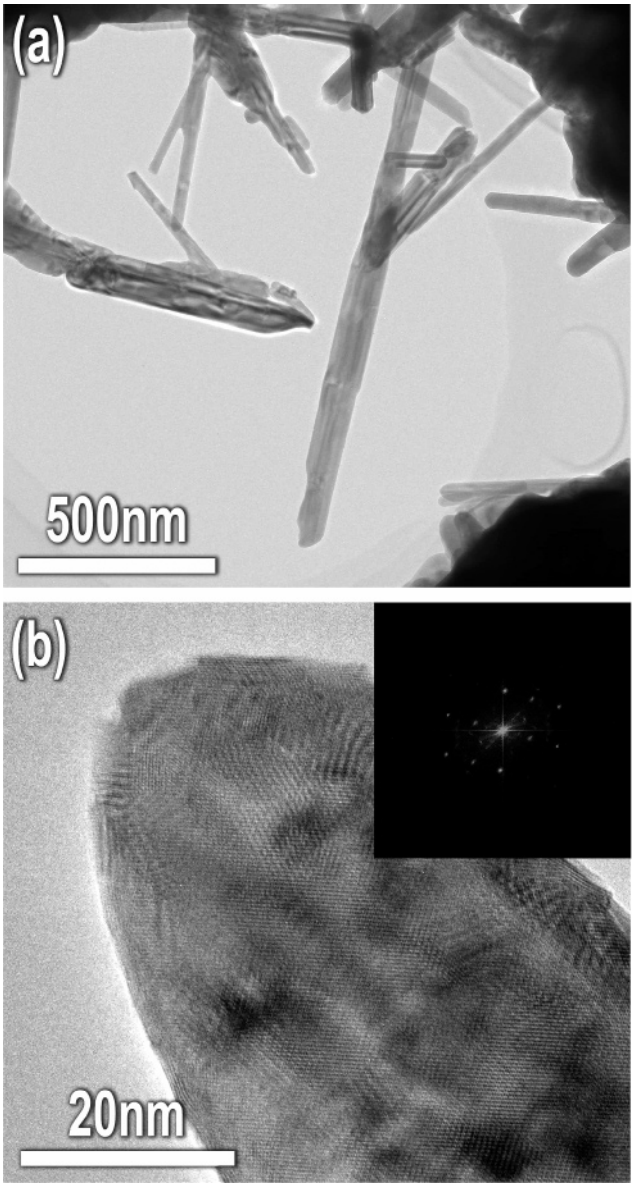

Figure 12. (a) TEM image of nanowires coming out of a dense oxide matrix. (b) High-resolution image of the tip of a single nanowire. The inset is a Fourier transform suggesting that the lattice in part b corresponds to 211 planes of the perovskite.

are rather stiff. The features displayed by the wires are quite similar to nanowires of perovskite $BaTiO_3$ reported by Park and co-workers.[27] At higher magnification (Figure 12b), the tip of a single wire, approximately 40 nm in diameter, is seen to comprise crystalline material with mostly Ba and Ce being seen in the EDX spectra. The inset is a Fourier transform suggesting that the lattice planes are perovskite 211. Because of the very large atomic numbers of Ba and Ce, none of the images displayed any evidence for features or particles that could be associated with the smaller *Z* fcc Pd seen in the XRD patterns.

To test the idea that the wires correspond to perovskite nucleated on and overgrowing small particles of palladium, we have performed some preliminary experiments on $BaCeO_3$ powders on which palladium was dispersed following which the material was heated in a reducing atmosphere. $BaCeO_3$ powders were added to a solution of the acetate $Pd(CH_3COO)_2$ in acetone, and after sonication for 1 h in an ultrasonic bath, the solvent was evaporated and the dried powder mixture was heated at 1000 °C for 1 h in flowing $5\%H_2/95\%N_2$. Figure 13 displays a SEM image of the powder after such heat treatment. It is seen that even after such a short heating in a reducing atmosphere, small rods of materials start growing out of the surfaces of the $BaCeO_3$ crystals. In the usual vapor−liquid−solid (VLS) mechanisms of nanowire growth, oxide materials such as ZnO can be nucleated and grow from small gold particles or droplets.[28] The process involves reducing ZnO to Zn, and it is the molten Zn that is transported through the gold droplets, where it alloys. As the Zn concentration in the Au−Zn alloy increases, it supersaturates, extrudes out from the droplet, and is oxidized to ZnO in the process. The process of perovskite nanowire growth seen here is believed to be

(27) Urban, J. F.; Spanier, J. E.; Ouyang, L.; Yun, W. S.; Park, H. *Adv. Mater.* **2003**, *15*, 423−426.

(28) Huang, M. H.; Wu, Y.; Feick, H.; Tran, N.; Weber, E.; Yang, P. *Adv. Mater.* **2001**, *13*, 113−116.

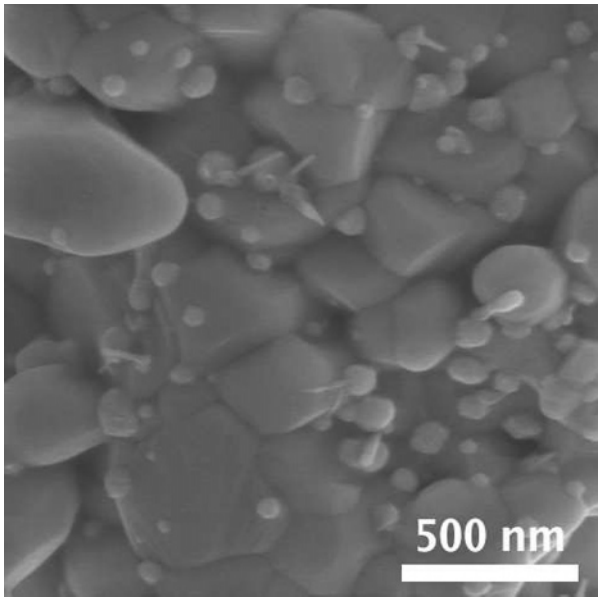

Figure 13. SEM image of $BaCeO_3$ powders on which palladium ions were deposited by evaporation of an acetone solution of $Pd(CH_3COO)_2$, followed by reduction at 1000 °C for 1 h under $5\%H_2/95\%N_2$. Initial stages of wire growth close to some of the smaller particles is observed.

similarly mediated by palladium particles. There are however many differences, including the absence of a vapor of liquid phase and the unlikelihood of alloy formation. Clearly the mechanism for wire formation requires deeper study, and whether it is a general feature of perovskite/noble metal systems requires exploration.

Conclusions

Using a carefully selected perovskite host, $BaCeO_3$, we provide convincing evidence that palladium can enter the lattice under oxidizing conditions forming $BaCe_{1-x}Pd_xO_{3-\delta}$ phases and then be induced to precipitate as fcc Pd. The results have profound implications to the design of new catalytic systems where the goal is frequently to avoid the sintering of noble metal particles. This system can also aid in improving our understanding of catalysis by noble metal ions doped in oxide hosts. We are currently exploring catalysis by the $BaCe_{1-x}Pd_xO_{3-\delta}$ system in both oxidized and reduced (two-phase) forms, as well as using crystal chemistry to devise new cyclable hosts for noble metal ions.

Acknowledgment. This work has been supported by the National Science Foundation (NSF) through the NER program (CTS05-08455) and the Department of Energy (DOE) Office of Basic Energy Sciences (BES) through grant DE FG02-05ER15725. K.P. thanks the NSF for support through an IGERT fellowship (DGE99-87618) and through a Graduate Student Fellowship. The work at UCSB made use of facilities of the Materials Research Laboratory, supported by the NSF (DMR05-20415). The work at the University of Pennsylvania was also supported in part by the National Science Foundation MRSEC Program, Grant DMR05-20020, and by the Air Force Office of Scientific Research, Material Command, USAF, under Grant FA9550-04-1-0077. Computational support was provided by a Challenge Grant from the High Performance Computing Modernization Office and by the NSF CRIF Program, Grant CHE-0131132. This work has benefited from the use of NPDF at the Lujan Center at Los Alamos Neutron Science Center, funded by DOE Office of Basic Energy Sciences. Los Alamos National Laboratory is operated by Los Alamos National Security LLC under DOE Contract No. DE-AC52-06NA25396. The upgrade of NPDF has been funded by NSF through Grant DMR00-76488.

CM062500I